

1 **Detailed dendritic excitatory/inhibitory balance through heterosynaptic**
2 **spike-timing-dependent plasticity**

3

4 Naoki Hiratani^{1,2*} and Tomoki Fukai¹

5 ¹Laboratory for Neural Circuit Theory, RIKEN Brain Science Institute, Hirosawa 2-1, Wako, Saitama,
6 Japan 351-0198

7 ²Current address: Gatsby Computational Neuroscience Unit, University College London, 25 Howland
8 Street, London, United Kingdom W1T 4JG

9 *Corresponding author: N.Hiratani@gmail.com

10

11 **Competing interests**

12 The authors have declared that no competing interests exist.

13

14 **Acknowledgments**

15 The authors thank to Dr. Laurent Venance for kindly providing the experimental data. This work was
16 partly supported by JSPS Doctorial Fellowship DC2 (NH), CREST JST, and KAKENHI No15H04265
17 and No16H01289 (TF).

18

19

20 **Abstract**

21 Balance between excitatory and inhibitory inputs is a key feature of cortical dynamics. Such balance
22 is arguably preserved in dendritic branches, yet its underlying mechanism and functional roles
23 remain unknown. Here, by considering computational models of heterosynaptic

24 spike-timing-dependent plasticity (STDP), we show that the detailed excitatory/inhibitory balance on
25 dendritic branch is robustly achieved through heterosynaptic interaction between excitatory and
26 inhibitory synapses. The model well reproduces experimental results on heterosynaptic STDP, and
27 provides analytical insights. Furthermore, heterosynaptic STDP explains how maturation of inhibitory
28 neurons modulates selectivity of excitatory neurons in critical period plasticity of binocular matching.
29 Our results propose heterosynaptic STDP as a critical factor in synaptic organization and resultant
30 dendritic computation.

31

32

33 **Significance statement**

34 Recent experimental studies have revealed that relative spike timings among neighboring
35 Glutamatergic and GABAergic synapses on a dendritic branch significantly influences changes in
36 synaptic efficiency of these synapses. This heterosynaptic form of spike-timing-dependent plasticity
37 (STDP) is potentially important for shaping the synaptic organization and computation of neurons,
38 but its functional role remains elusive. Here, through computational modeling, we show that
39 heterosynaptic plasticity causes the detailed balance between excitatory and inhibitory inputs on the
40 dendrite, at the parameter regime where previous experimental results are well reproduced. Our
41 result reveals a potential principle of GABA-driven neural circuit formation.

42

43

44 **Introduction**

45 Activity dependent synaptic plasticity is essential for learning. Especially, spike time difference
46 between presynaptic and postsynaptic neurons is a crucial factor for synaptic learning (Bi and Poo,

47 1998)(Caporale and Dan, 2008). Recent experimental results further revealed that the relative spike
48 timings among neighboring synapses on a dendritic branch have significant influence on changes in
49 synaptic efficiency of these synapses (Tsukada et al., 2005)(Hayama et al., 2013)(Paille et al.,
50 2013)(Oh et al., 2015)(Bazelot et al., 2015). Especially, the timing of GABAergic input exerts a great
51 impact on synaptic plasticity at nearby glutamatergic synapses. Similar phenomenon were also
52 observed in biophysical simulations (Cutsuridis, 2011)(Bar-Ilan et al., 2013). This heterosynaptic
53 form of spike-timing-dependent plasticity (h-STDP) is potentially important for synaptic organization
54 on dendritic tree, and resultant dendritic computation (Mel and Schiller, 2004)(Branco et al., 2010).
55 However, the functional role of h-STDP remains elusive, partly due to lack of simple analytical model.

56 In the understanding of homosynaptic STDP, simple mathematical formulation of plasticity
57 has been playing important roles (Gerstner et al., 1996)(Song et al., 2000)(Vogels et al., 2011).
58 Motivated by these studies, we constructed a mathematical model of h-STDP based on
59 calcium-based synaptic plasticity models (Shouval et al., 2002)(Graupner and Brunel, 2012), and
60 then considered potential functional merits of the plasticity. The model reproduces several effects of
61 h-STDP observed in the hippocampal CA1 area and the striatum of rodents (Hayama et al.,
62 2013)(Paille et al., 2013), and provides analytical insights for the underlying mechanism. The model
63 further indicates that h-STDP causes the detailed balance between excitatory and inhibitory inputs
64 on a dendritic branch owing to the inhibitory inputs that shunt long-term depression (LTD) at
65 neighboring correlated excitatory synapses. This result suggests that not only the number and the
66 total current of excitatory/inhibitory synapses are balanced at a branch (Liu, 2004)(Wilson et al.,
67 2007), but temporal input structure is also balanced as observed in the soma (Dorrn et al.,
68 2010)(Froemke, 2015). Moreover, by considering dendritic computation, we show that such detailed
69 balance is beneficial for detecting changes in input activity. The model also reconciles with critical

70 period plasticity of binocular matching observed in V1 of mice (Wang et al., 2010)(Wang et al., 2013),
71 and provides a candidate explanation on how GABA-maturation modulates the selectivity of
72 excitatory neurons during development.

73

74

75 **Methods**

76 In this study, we first constructed a model of dendritic spine, then based on that model, built models
77 of a dendritic branch, and a dendritic neuron. We also created an analytically tractable model of a
78 spine, by reducing the original spine model.

79

80 *Spine model: Calcium-based STDP model with current-based heterosynaptic interaction*

81 Let us first consider membrane dynamics of a dendritic spine. Membrane potential of a
82 spine is mainly driven by presynaptic inputs through AMPA/NMDA receptors, backpropagation of
83 postsynaptic spike, leaky currents, and current influx/outflux caused by excitatory/inhibitory synaptic
84 inputs at nearby synapses. Hence, we modeled membrane dynamics of spine i with the following
85 differential equation:

$$86 \frac{du_i(t)}{dt} = -\frac{u_i(t)}{\tau_m} + \gamma_A x_i^A(t) + \gamma_N g_N(u_i) x_i^N(t) + \gamma_{BP} x_i^{BP}(t) - \gamma_I \sum_{j \in \Omega_i^I} x_j^I(t - d_I) + \gamma_E \sum_{j \in \Omega_i^E} x_j^E(t - d_E), \quad (1)$$

87 where u_i is the membrane potential of the spine, and τ_m is the membrane time constant(see **Table 1**
88 for definitions of variables). Here, conductance changes were approximated by current changes. The
89 resting potential was renormalized to zero for simplicity. In next terms, x_i^A and x_i^N are glutamate
90 concentration on AMPA/NMDA receptors respectively. The function $g_N(u_i) = \alpha_N u_i + \beta_N$ represents
91 voltage dependence of current influx through NMDA receptors. This positive feedback is enhanced
92 when additional current is provided through back-propagation. As a result, the model reproduces

93 large depolarization caused by coincident spikes between presynaptic and postsynaptic neurons.
94 Although AMPA receptor also shows voltage dependence, here we neglected the dependence, as
95 the relative change is small around the resting potential (Lüscher and Malenka, 2012). x_i^{BP} is the
96 effect of backpropagation from soma, and the last two terms of the equation represents
97 heterosynaptic current, which is given as the sum of inhibitory (excitatory) currents x_j^I (x_j^E) at nearby
98 synapses. We defined sets of nearby inhibitory/excitatory synapses as Ω_i^I and Ω_i^E respectively, and
99 their delays were denoted as d_I and d_E . Each input x_i^Q ($Q = A, N, BP, I, E$) is given as convoluted
100 spikes:

$$101 \quad \frac{dx_i^Q(t)}{dt} = -\frac{x_i^Q(t)}{\tau_Q} + \sum_{s^k} \delta(t - s^k), \quad (2)$$

102 where s^k represents the spike timing of the k -th spike. In the simulation, although convolution is
103 calculated at the heterosynaptic synapse, this does not influence results because exponential decay
104 is linear.

105 We next consider calcium influx to a spine through NMDA receptors and VDCC. For a
106 given membrane potential u_i , calcium concentration at spine i can be written as

$$107 \quad \frac{dc_i}{dt} = -\frac{c_i}{\tau_C} + g_N(u_i)x_i^N(t) + g_V(u_i), \quad (3)$$

108 where $g_V(u_i) = \alpha_V u_i$ represents calcium influx through VDCC, and $g_N(u_i)x_i^N(t)$ is the influx from NMDA.

109 Calcium concentration at spine is the major indicator of synaptic plasticity, and many
110 results indicate that high Ca^{2+} concentration on a spine typically induces LTP, while low
111 concentration often causes LTD (Lüscher and Malenka, 2012). Previous modeling studies revealed
112 calcium-based synaptic plasticity model constructed on that principle well replicate various
113 homosynaptic STDP time window observed in *in vitro* experiments (Shouval et al., 2002)(Graupner
114 and Brunel, 2012). Hence, here we employed their framework for plasticity model. We additionally

115 introduced an intermediate variable to reflect all-or-none nature of synaptic weight change (Petersen
116 et al., 1998). This variable approximately represents the concentration of plasticity related enzymes
117 such as CaMKII or PP1 (Graupner and Brunel, 2007). In the proposed model the intermediate y_i and
118 synaptic weight w_i follow

$$119 \quad \frac{dy_i(t)}{dt} = -\frac{y_i(t)}{\tau_y} + C_p [c_i - \theta_p]_+ - C_d [c_i - \theta_d]_+, \quad (4)$$

$$120 \quad \frac{dw_i(t)}{dt} = B_p [y_i - y_{th}]_+ - B_d [-(y_i + y_{th})]_+. \quad (5)$$

121 $[X]_+$ is a sign function which returns 1 if $X \geq 0$, returns 0 otherwise. Note that, in this model setting, as
122 observed in recent experiments (Gambino et al., 2014), back-propagation is not necessary for LTP, if
123 presynaptic inputs are given when the membrane potential at the spine is well depolarized.

124 In the simulation, we set common parameters as $\tau_C=18.0\text{ms}$, $\tau_M=3.0\text{ms}$, $\tau_N=15.0\text{ms}$,
125 $\tau_A=3.0\text{ms}$, $\tau_{BP}=3.0\text{ms}$, $\tau_I=3.0\text{ms}$, $\tau_E=6.0\text{ms}$, $\tau_Y=50\text{s}$, $d_f=0.0\text{ms}$, $\alpha_N=1.0$, $\beta_N=0.0$, $\alpha_V=2.0$, $\gamma_A=1.0$,
126 $\theta_p=70$, $\theta_d=35$, $C_d=1.0$, $B_p=0.001$, $B_d=0.0005$. Note that due to positive feedback between equations
127 (1) and (3), effective timescales of calcium dynamics and NMDA channel become longer than the
128 given values. In the model of STDP at striatum, in addition, we used $\gamma_N=0.05$, $\gamma_{BP}=8.0$, $\gamma_I=5.0$, $C_p=2.3$,
129 $y_{th}=250$, while for the model of Schaffer collateral synapses, we used $\gamma_N=0.2$, $\gamma_{BP}=8.5$, $\gamma_I=3.0$, $C_p=2.2$,
130 $y_{th}=750$, $d_E=1.0$, $\gamma_E=1.0$. In the parameter search, decay time constants were chosen from
131 biologically reasonable ranges (Koch, 1998), α_N , γ_A , C_d , B_d were fixed at unitary values, and other
132 parameters were manually tuned. Subsequently, robustness of parameter choice was confirmed
133 numerically (Fig. 3). Synaptic weight variables $\{w\}$ were bounded to $0 < w < 500$, and initialized at $w =$
134 100. All other variables were initialized at zero in the simulation. Paired stimulation was given every 1
135 second for 100 seconds, and synaptic weight changes were calculated from the values 400 seconds
136 after the end of stimulation. In the cortico-striatal synapse model, the inhibitory spike was presented

137 at the same timing with the presynaptic spike, and for Schaffer collateral synapses, inhibitory spikes
138 were given 10 milliseconds before pre (post) spikes in pre-post (post-pre) stimulation protocols. In
139 calculation of intermediate variable $y(t)$ in Figures 2B,D, we ignored the effect of exponential decay,
140 because of the difference in timescale ($\tau_y \gg 1$ seconds). We subtracted 7.5 milliseconds of axonal
141 delay from the timing of presynaptic stimulation in the calculation of spike timing difference.

142

143 *Dendritic hotspot model*

144 Dendritic hotspot model was constructed based on the Schaffer collateral synapse model described
145 above. For simplicity, we hypothesized that heterosynaptic current due to inhibitory spike arrives on
146 excitatory spines at the same time, and also disregarded E-to-E interaction by setting $\gamma_E=0.0$.
147 Correlated spikes were generated using hidden variables as in previous studies (Vogels et al.,
148 2011)(Hiratani and Fukai, 2015). We generated five dynamic hidden variables, and updated them at
149 each time step by $s_\mu(t + \Delta t) = (\zeta - \frac{1}{2})(1 - \alpha_s) + s_\mu(t)\alpha_s$, where $\alpha_s = \exp[-\Delta t/\tau_s]$, $\tau_s=10\text{ms}$,
150 $\mu=0,1,\dots,4$, and ζ is a random variable uniformly chosen from $[0,1)$. In the simulation, the time step
151 was set at $\Delta t=0.1\text{ms}$. Activities of presynaptic neurons were generated by rate-modulated Poisson
152 process with $r_i^E(t) = r_X^E + r_S^E s_\mu(t)$ for excitatory neuron i modulated by the hidden variable μ (due to
153 non-negative constraint on $r_i^E(t)$, we set $r_i^E(t) = 0$ when $r_X^E + r_S^E s_\mu(t) < 0$). Similarly, the
154 presynaptic inhibitory neuron was described by a Poisson-model with $r^I(t) = r_X^I + r_S^I s_0(t)$. Activity of
155 the postsynaptic neuron was given as a Poisson-model with a fixed rate r_{post} . We set parameters $\{r_X^E,$
156 $r_S^E, r_{post}\}$ in a way that all pre and postsynaptic excitatory neurons show the same average firing rate
157 at 5Hz, to avoid the effect of firing-rate difference on synaptic plasticity.

158 For parameters, we used $\gamma=1.2$, $\beta_N=1.0$, $\gamma_{BP}=8.0$, $C_p=2.11$, $y_{th}=250$ and other parameters
159 were kept at the same value with the original Schaffer collateral model. Except for Figure 5D, the

160 delay of inhibitory spike was set as zero. Presynaptic activities were given by $r_X^E=1.0\text{Hz}$, $r_S^E=500.0$,
 161 $r_X^I=2.0\text{Hz}$, $r_S^I=1000.0$, and postsynaptic firing rate was set as $r_{post} = 5.0\text{Hz}$. In Figure 5C, the
 162 correlation was calculated between dendritic membrane potential $g_b(u_b)$ and hidden variables $\{s_\mu(t)\}$,
 163 where $u_b(t) \equiv \sum_{i=1}^{10} w_i u_i(t) / (w_o^E N_b^E)$, and $g_b(u)$ was defined as $g_b(u)=u$ if $u > u_b^o$, otherwise $g_b(u)=u_b^o$
 164 with $u_b^o=-5.0$.

165

166 *Two-layered neuron model*

167 Previous studies suggest that complicated dendritic computation can be approximated by a
 168 two-layered single cell model (Poirazi et al., 2003)(London and Häusser, 2005). Thus, we
 169 constructed a single cell model by assuming that each hotspot works as a subunit of a two-layered
 170 model. We defined the mean potential of a dendritic subunit k by $u_b^k(t) \equiv \sum_{i=1}^{N_b^E} w_i^k u_i^k(t) / (w_o^E N_b^E)$, and
 171 calculated the somatic membrane potential by $u_{soma}(t) \equiv \sum_{k=1}^K g_b(u_b^k(t))$. Postsynaptic spikes were
 172 given as a rate-modulated Poisson model with the rate $u_{soma}(t)/I_{dv}(t)$. $I_{dv}(t)$ is the divisive inhibition
 173 term introduced to keep the output firing rate at r_{post} . By using the mean somatic potential
 174 $\frac{d\bar{u}_{soma}(t)}{dt} = -\frac{\bar{u}_{soma}(t) - u_{soma}(t)}{\tau_v}$, $I_{dv}(t)$ was calculated as $I_{dv}(t) \equiv \bar{u}_{soma}(t) / r_{post}$.

175 In the simulations described in Figure 6, we used $C_p=2.01$, $\tau_v=1\text{s}$, $K=100$, and other
 176 parameters were kept at the same values with the dendritic hotspot model. During the learning
 177 depicted in Figure 6BC, we used the same input configuration with the dendritic hotspot model. In
 178 Figure 6DE, The activity levels of hidden variables $\{s_\mu(t)\}$ were kept at a constant value ($s_\mu(t)=0.25$)
 179 during 500ms stimulation, and otherwise kept at zero. Additionally, inhibitory presynaptic activities
 180 were set as $r_X^I=10\text{Hz}$, $r_S^I=2000$. In Figure 6D, we modulated firing rates of both excitatory and
 181 inhibitory presynaptic neurons, by changing the activity levels of hidden variables $\{s_\mu(t)\}$ from 0.1 to

182 0.5. The ratio of change detecting spikes was defined as the ratio of spikes occurred within 50
 183 milliseconds from the change to the total spike count.

184 For the model of critical period plasticity of binocular matching depicted in Figure 7, we also
 185 used the two-layered single cell model. The neuron model has $K=100$ dendritic branches, each
 186 receives $N_b^E=20$ excitatory inputs and 1 inhibitory input. At each branch, half of excitatory inputs are
 187 from the contralateral eye, and the other half are from the ipsilateral eye. Each excitatory input
 188 neuron have direction selectivity characterized with $\theta_{k,i}^E$, and shows rate-modulated Poisson firing
 189 with

$$190 \quad r_{k,i} = r_x^E \exp\left[\beta_E \cos(\theta(t) - \theta_{k,i}^Q)\right] / I_0(\beta_E)$$

191 where $\theta(t)$ is the direction of the visual stimulus at time t , Q is either contra- or ipsilateral, and $I_0(\beta_E)$ is
 192 the modified Bessel function of order 0. Similarly, firing rate of an inhibitory neuron was given as

$$193 \quad r_k^I(t) = r_x^I \exp\left[\beta_I \cos(\theta(t) - \theta_k^I)\right] / I_0(\beta_I).$$

194 For each excitatory input neuron, mean direction selectivity $\{\theta_{k,i}^Q\}$ was randomly chosen from a von Mises distribution $\exp\left[\beta_S \cos(\theta_{k,i}^Q - \theta_Q)\right] / 2\pi I_0(\beta_S)$, where

195 $Q=\{\text{contra, ipsi}\}$. In the simulation, we used $\theta_{\text{contra}}=-\pi/4$, $\theta_{\text{ipsi}}=\pi/4$. Correspondingly, mean direction

196 selectivity of a inhibitory neuron $\{\theta_k^I\}$ was defined as the mean of its selectivity for ipsi- and

197 contralateral inputs (ie. $\theta_k^I = (\theta_k^{I,ipsi} + \theta_k^{I,contra})/2$), where $\theta_k^{I,ipsi}$ and $\theta_k^{I,contra}$ were also randomly depicted

198 from $\exp\left[\beta_S \cos(\theta_k^Q - \theta_Q)\right] / 2\pi I_0(\beta_S)$. Direction of visual stimulus $\theta(t)$ changes randomly with

199 $\theta(t + \Delta t) = \theta(t) + \sigma_{sr} \zeta_G$ where ζ_G is a Gaussian random variable, and Δt is the time step of the

200 simulation. To mimic monocular deprivation, in the shadowed area of Figure 7E, we replaced

201 contra-driven input neuron activity with a Poisson spiking with constant firing rate r_{md}^E . In addition, to

202 simulate the lack of contra-driven inputs to inhibitory neurons, we replaced inhibitory activity with

203 $r'_k(t) = r'_{md} + (r'_x/2)\exp[\beta_l \cos(\theta(t) - \theta_k^{l,ipsi})]/I_0(\beta_l)$. Similarly, in Figure 7C, we measured direction
 204 selectivity by providing monocular inputs, while replacing the inputs from the other eye with a
 205 homogeneous Poisson spikes with firing rate r_{md}^E .

206 To evaluate the development of binocular matching, we introduced three order parameters.
 207 First, the difference between mean excitatory direction selectivity and inhibitory selectivity at a
 208 branch k was evaluated by $\theta_{b,k}^d = \left| \arg\left(\sum_i w_{k,i}^E e^{i(\theta_{k,i}^E - \theta_k^l)}\right) \right|$. Similarly, the global direction selectivity
 209 difference between inputs from the ipsi- and contralateral eyes were defined by

$$210 \quad \theta_G^d = \hat{d} \left[\arg\left(\sum_{k=1}^K \sum_{i \in ipsi} w_{k,i}^E e^{i\theta_{k,i}^E}\right), \arg\left(\sum_{k=1}^K \sum_{i \in contra} w_{k,i}^E e^{i\theta_{k,i}^E}\right) \right], \quad (6)$$

211 where the function $\hat{d}[\theta_1, \theta_2]$ calculates the phase difference between two angles. Finally, direction
 212 selectivity index DSI for binocular input was calculated by

$$213 \quad DSI = \left| \frac{\sum_{k=1}^K \sum_{i=1}^{N_b^E} w_{k,i}^E e^{i\theta_{k,i}^E}}{\sum_{k=1}^K \sum_{i=1}^{N_b^E} w_{k,i}^E} \right|. \quad (7)$$

214 For the calculation of the monocular direction selectivity index, at each branch k , we took sum over
 215 $N_b^E/2$ excitatory inputs corresponding to each eye instead of all N_b^E inputs.

216 In the simulation, we set $\gamma_I=2.5$, $C_p=1.85$, $y_{th}=750.0$, $u_b^o=0.0$, and the rest of parameters
 217 were kept at the values used in the dendritic hotspot model. Inputs parameters were set at $\beta_E=4.0$,
 218 $\beta_I=2.0$, $\beta_S=1.0$, $\theta_{contra}=-\pi/4$, $\theta_{ipsi}=\pi/4$, $r_X^E=5.0$, $r_X^I=10.0$, $r_{md}^E=1.0$, $r_{md}^I=1.0$, and $\sigma_{sr} = 0.1\sqrt{\Delta t}$.

219

220 *Reduced model*

221 If we shrink equations for membrane potential (eq. 1) and calcium concentration (eq. 3) into one, the
 222 reduced equation would be written as,

$$\begin{aligned} \frac{dC_i(t)}{dt} = & -\frac{C_i(t)}{\tau_C} + C_{pre} X_i(t) + C_{post} [1 + g_C(C_i(t - \Delta t))] X_{post}(t) \\ & - C_I \sum_{j \in \Omega_I^I} X_j^I(t - d_I) + C_E \sum_{j \in \Omega_I^E} X_j^E(t - d_E), \end{aligned} \quad (8)$$

where $g_c(X) = [X]_+ \eta X$ captures the nonlinear effect caused by pre-post coincidence (i.e. $g_c(X)$ returns ηX if $X > 0$, otherwise returns 0). All inputs X_i , X_{post} , X_j^I , X_j^E were given as point processes, and d_I , d_E are heterosynaptic delays. g_c was calculated from the value of C_i at $t = t - \Delta t$ to avoid pathological divergence due to the point processes. In the simulation, we simply used value of C_i one time step before. For the intermediate y , we used the same equation as before. Note that above equation is basically same with the one in (Graupner and Brunel, 2012) except for the nonlinear term $g_c(C)$ and the heterosynaptic terms.

Let us consider weight dynamics of an excitatory synapse that has only one inhibitory synapse in its neighbor. For analytical tractability, we consider the case when presynaptic, postsynaptic, and inhibitory neurons fire only one spikes at $t = t_{pre}$, t_{post} , t_I respectively. In case of the CA1 experiment, because GABA uncaging was always performed before pre and postsynaptic spike, the timing of inhibitory spike is given as $t_I = \min(t_{pre}, t_{post}) - \bar{\delta}_I$ for $\bar{\delta}_I > 0$. In this setting, the change in intermediate variable of the excitatory synapse is given as

$$\Delta y = \begin{cases} G_1(C_1, t_{pre} - t_{post}) + G_2(C_{pre} + C_1 e^{-(t_{pre} - t_{post})/\tau_C}) & (\text{if } t_{post} < t_{pre}) \\ G_1(C_2, t_{post} - t_{pre}) + G_2(C_{post} [1 + g_C(C_2 e^{-(t_{post} - t_{pre})/\tau_C})] + C_2 e^{-(t_{post} - t_{pre})/\tau_C}) & (\text{otherwise}) \end{cases}$$

where,

$$C_1 \equiv C_{post} - C_I e^{-(t_{post} - t_I)/\tau_C}, \quad C_2 \equiv C_{pre} - C_I e^{-(t_{pre} - t_I)/\tau_C}$$

$$\begin{aligned} G_1(C, \Delta t) \equiv & B_p [C - \theta_p]_+ \left(\left[\tau_C \log \frac{C}{\theta_p} - \Delta t \right]_+ \Delta t + \left[\Delta t - \tau_C \log \frac{C}{\theta_p} \right]_+ \tau_C \log \frac{C}{\theta_p} \right) \\ & - B_d [C - \theta_d]_+ \left(\left[\tau_C \log \frac{C}{\theta_d} - \Delta t \right]_+ \Delta t + \left[\Delta t - \tau_C \log \frac{C}{\theta_d} \right]_+ \tau_C \log \frac{C}{\theta_d} \right), \end{aligned}$$

241
$$G_2(C) \equiv B_p [C - \theta_p]_+ \tau_C \log \frac{C}{\theta_p} - B_d [C - \theta_d]_+ \tau_C \log \frac{C}{\theta_d}.$$

242 Similarly, in case of the striatum experiment, by setting $\eta=0$, the change in the intermediate variable
 243 is given as

244
$$\Delta y = \begin{cases} G_1(C_{post}, t_{pre} - t_{post}) + G_1(C_3, t_I - t_{pre}) + G_2(-C_I + C_3 e^{-(t_I - t_{pre})/\tau_C}) & (\text{if } t_{post} < t_{pre} < t_I) \\ G_1(C_{pre}, t_I - t_{pre}) + G_1(C_4, t_{post} - t_I) + G_2(C_{post} + C_4 e^{-(t_{post} - t_I)/\tau_C}) & (\text{if } t_{pre} < t_I < t_{post}) \\ G_1(C_{pre}, t_{post} - t_{pre}) + G_1(C_5, t_I - t_{post}) + G_2(-C_I + C_5 e^{-(t_I - t_{post})/\tau_C}) & (\text{if } t_{pre} < t_{post} < t_I), \end{cases}$$

245 where

246
$$C_3 \equiv C_{pre} + C_{post} e^{-(t_{pre} - t_{post})/\tau_C}, \quad C_4 \equiv -C_I + C_{pre} e^{-(t_I - t_{pre})/\tau_C}, \quad \text{and} \quad C_5 \equiv C_{post} + C_{pre} e^{-(t_{post} - t_{pre})/\tau_C}.$$

247 In the simulation, parameters were set at $\tau_C=30\text{ms}$, $C_{post}=2.0$, $\theta_p=1.6$, $\theta_d=1.0$, $B_p=2.25$,
 248 $B_d=1.0$. Additionally, in the model of a Schaffer collateral synapse, we used $\delta_f=1.0$, $C_{pre}=1.0$, $C_E=0.30$,
 249 $\eta=2.0$, and for the model of a cortico-striatal synapse, we employed $\delta_f=5.0$, $C_{pre}=0.75$, $C_E=0.0$, $\eta=0.0$.
 250 In Figures 3C and D, we used the parameter set for the model of Schaffer collateral synapse.

251 As depicted in Figure 3D, the model also provides an analytical insight to E-to-E interaction,
 252 in addition to I-to-E interaction analyzed in the main result. In E-to-E interaction, neighboring
 253 synapses receive small heterosynaptic calcium transient C_E instead of presynaptic input C_{pre} . Thus,
 254 we can characterize the shapes of STDP time windows by the heterosynaptic excitatory effect
 255 parameter C_E , and postsynaptic effect parameters C_{post} (Fig. 3D). When the postsynaptic effect
 256 parameter C_{post} satisfies $\theta_p < C_{post} < \theta_p + C_I e^{-\delta_I/\tau_C}$, and the heterosynaptic effect parameter C_E
 257 fulfills $C_I e^{-\delta_I/\tau_C} < C_E < \theta_p$, STDP time window shows Hebbian-type timing dependency
 258 (upper-middle orange-colored region in Fig. 3D). On the other hand, if C_E is smaller than $C_I e^{-\delta_I/\tau_C}$
 259 while satisfying $\theta_p + C_I e^{-\delta_I/\tau_C} - C_{post} < C_E$, then the STDP curve becomes LTD dominant (upper-left
 260 green-colored region in Fig. 3D) as observed in experiments (Hayama et al., 2013)(Oh et al., 2015).

261 Excitatory heterosynaptic effect C_E is expectedly smaller than the inhibitory effect C_I , because the
262 inhibitory potential is typically more localized (Gidon and Segev, 2012). Thus, $C_E < C_I e^{-\delta_i/\tau_c}$ is also
263 expected to hold for small δ_i , suggesting robust heterosynaptic LTD at neighboring synapses.

264

265

266 **Results**

267 *Calcium-based synaptic plasticity model with current-based heterosynaptic interaction explains*
268 *h-STDP.*

269 We constructed a model of a dendritic spine as shown in Figure 1A (see *Spine model* in *Methods* for
270 details). In the model, the membrane potential of the spine $u(t)$ is modulated by influx/outflux from
271 AMPA/NMDA receptors (x^A and $g_N(u)x^N$ in Fig. 1A), back-propagation (x^{BP}), and heterosynaptic
272 currents from nearby excitatory/inhibitory synapses (x^E and x^I) (see **Table 1** for the definitions of
273 variables). Calcium concentration in the spine $c(t)$ is controlled through NMDA receptors and
274 voltage-dependent calcium channels (VDCC) $g_V(u)$ (Higley and Sabatini, 2012). Because both NMDA
275 and VDCC are voltage-dependent (Lüscher and Malenka, 2012), the calcium level in the spine is
276 indirectly controlled by pre, post, and heterosynaptic activities (Fig. 1B top and middle panels). For
277 synaptic plasticity, we used calcium-based plasticity model, in which LTP/LTD are initiated if the Ca^{2+}
278 level is above LTP/LTD thresholds (orange and cyan lines in Fig. 1B middle). This plasticity model is
279 known to well capture homosynaptic STDP (Shouval et al., 2002)(Graupner and Brunel, 2012). We
280 introduced an intermediate variable $y(t)$ to capture non-graded nature of synaptic weight change
281 (Petersen et al., 1998). Thus, changes in Ca^{2+} level are first embodied in the intermediate $y(t)$ (Fig.
282 1B bottom), and then reflected to the synaptic weight $w(t)$ upon accumulation. The intermediate
283 variable $y(t)$ is expected to correspond with concentration of plasticity related enzymes such as

284 CaMKII or PP1 (Graupner and Brunel, 2007).

285 We first consider the effect of inhibitory input to synaptic plasticity at nearby excitatory
286 spines. A recent experimental result revealed that, in medium spiny neuron, synaptic connections
287 from cortical excitatory neurons typically show anti-Hebbian type STDP under pairwise stimulation
288 protocol, but if GABA-A receptor is blocked, STDP time window flips to Hebbian (Paille et al., 2013)
289 (points in Fig. 2A). The proposed model can explain this phenomenon in the following way. Let us
290 first consider the case when the presynaptic excitatory input arrives before the postsynaptic spike. If
291 the GABAergic input is blocked, presynaptic and postsynaptic spikes jointly cause a large membrane
292 depolarization at the excitatory spine. Subsequently, the calcium concentration rises up above the
293 LTP threshold (red line in Fig 2B upper-right), hence inducing LTP after repetitive stimulation (red line
294 in Fig 2B lower-right). In contrast, if the GABAergic input arrives coincidentally with the presynaptic
295 input, depolarization at the excitatory spine is attenuated by negative current influx through the
296 inhibitory synapse. As a result, calcium concentration cannot go up beyond the LTP threshold
297 although it is still high enough to eventually cause LTD (black lines in Fig 2B right). Similarly when
298 the postsynaptic spike arrives to the spine before the presynaptic spike does, without any GABAergic
299 input, the presynaptic spike causes slow decay in the level of calcium concentration that may induce
300 LTD (red lines in Fig 2B left). On the contrary, if the GABAergic input is provided simultaneously with
301 the presynaptic input, slow decay in the calcium concentration is blocked because the inhibitory input
302 causes hyperpolarization of the membrane potential at the excitatory spine. As a result, LTP is more
303 likely achieved (black lines in Fig. 2B left). Therefore, when a GABAergic input arrives in coincidence
304 with a presynaptic excitatory input, the STDP time window changes its sign in both pre-post and
305 post-pre regimes (lines in Fig. 2A).

306 GABAergic effect on excitatory synaptic plasticity is also observed in CA1 (Hayama et al.,

2013). In this case, post-pre stimulation does not induce LTD unless GABA uncaging is conducted near the excitatory spine right before the postsynaptic spike arrives at the spine, whereas LTP is induced by pre-post stimulation regardless of GABA uncaging (blue and cyan points in Fig. 2C). The proposed model can also replicate these results. In pre-post stimulation, due to positive feedback through NMDA receptor, the membrane potential of the spine shows strong depolarization even if inhibitory current is delivered through GABA uncaging (solid and dotted blue lines in Fig. 2D upper-right). Thus, LTP is caused after repetitive stimulation (blue lines in Fig. 2D lower-right). By contrast, in post-pre protocol, LTP/LTD effects tend to cancel each other in the absence of GABAergic input, whereas LTD becomes dominant under the influence of GABAergic input (dotted and solid blue lines in Fig. 2D left, respectively).

In addition to inhibitory-to-excitatory effect, excitatory-to-excitatory (E-to-E) effect is also observed in case of CA1 (Hayama et al., 2013). If GABA uncaging is performed right before postsynaptic firing, LTD is also observed in neighboring excitatory spines (green point in Fig. 2C right). This E-to-E heterosynaptic effect is not observed in the absence of GABAergic input (green points in Fig 2C left). Correspondingly, in the model, excitatory current influx from a nearby synapse causes mild potentiation of calcium concentration in cooperation with inhibitory current influx, hence eventually induces LTD (green lines in Fig 2D left). Note that for this E-to-E effect, interaction at latter stage of synaptic plasticity may also play a dominant role (Hayama et al., 2013).

The obtained results are mostly robust against parameter change, as long as associated parameter values satisfy certain relationships (Fig. 3A). In addition, we found that the coefficient for heterosynaptic inhibitory effect should be larger for fitting the result from the striatum experiment, compared to CA1 (Fig. 3B top). This is consistent with strong inhibition observed in striatum (Mallet et al., 2005). We also found that for reproducing the result from the CA1 experiment, a high

330 NMDA/AMPA ratio is crucial, while the striatum model is rather robust against it, as long as calcium
 331 influx/outflux is modulated by NMDA receptors (Fig. 3B bottom).

332

333 *Phase transitions underlying h-STDP*

334 In the previous section, we introduced a biophysical model to establish its relevance to the
 335 corresponding biological processes and get insight into the underlying mechanism. However, not all
 336 components of the model are necessary to reproduce the observed properties of h-STDP. Here, we
 337 provide a simple analytically tractable model to investigate the generality of the proposed
 338 mechanism.

339 To this end, we simplify the model to the one in which calcium level at a spine is directly
 340 modulated by pre-, post-, and heterosynaptic activities as given below,

$$\begin{aligned}
 \frac{dC_i(t)}{dt} = & -\frac{C_i(t)}{\tau_C} + C_{pre} X_i(t) + C_{post} [1 + g_C(C_i(t - \Delta t))] X_{post}(t) \\
 & - C_I \sum_{j \in \Omega_i^I} X_j^I(t - d_j) + C_E \sum_{j \in \Omega_i^E} X_j^E(t - d_E).
 \end{aligned}
 \tag{9}$$

342 Here, $C_i(t)$ represents Ca^{2+} concentration at spine i , X_i and X_{post} represent presynaptic and
 343 postsynaptic spikes respectively, d_I and d_E are heterosynaptic delays, and Ω_i^I and Ω_i^E are the sets of
 344 neighboring inhibitory and excitatory synapses (see *Reduced model* in *Methods* for the details of the
 345 model). Despite simplicity, the model can qualitatively reproduce heterosynaptic effects observed in
 346 striatal and CA1 neurons, though the quantitative accuracy is degraded (Fig. 4A and B respectively).
 347 Importantly, the reduced model provides further analytical insights into the phenomena.

348 Let us consider how the inhibitory effect parameter C_I controls I-to-E heterosynaptic effect
 349 observed in the CA1 experiment. If we characterize the shape of STDP time windows by the total
 350 number of its local minimum/maximum, the parameter space can be divided into several different

351 phases (Fig. 4C). If LTP threshold θ_p satisfies $C_{pre} < \theta_p < C_{post}$, Hebbian type STDP time window
352 appears when the strength of heterosynaptic inhibitory effect C_I satisfies
353 $(C_{post} - \theta_p)e^{\delta_I/\tau_C} < C_I < C_{pre}e^{\delta_I/\tau_C}$ (upper orange-colored region in Fig. 4C; see *Methods* for the
354 details of analysis). Here we defined δ_I as the spike timing difference between inhibitory spike and
355 presynaptic (postsynaptic) spikes in pre-post (post-pre) stimulation protocols. If C_I is larger than
356 $C_{pre}e^{\delta_I/\tau_C}$, a strong inhibitory effect causes LTD even in the pre-post regime (green-colored
357 region in Fig. 4C), whereas LTD in the post-pre regime is suppressed when C_I is smaller than
358 $(C_{pre} - \theta_p)e^{\delta_I/\tau_C}$ (gray-colored region in Fig. 4C). Thus, heterosynaptic LTD observed in Figure 2C
359 can be understood as the phase shift from the gray-colored region to the orange-colored region in
360 Figure 4C, due to change in the inhibitory effect C_I . This analysis further confirms that, for induction
361 of heterosynaptic LTD, the heterosynaptic spike timing difference δ_I should be smaller than the
362 timescale of Ca^{2+} dynamics τ_C (Hayama et al., 2013). This is because $\delta_I < \tau_C \log\left(\frac{C_I}{C_{post} - \theta_p}\right)$ is
363 necessary for a significant heterosynaptic LTD, and typically C_I is smaller than C_{post} and θ_p . In
364 addition, heterosynaptic suppression of pre-post LTP (green-colored region) is very unlikely to
365 happen because $C_I > C_{pre}e^{\delta_I/\tau_C}$ is necessary. This condition is difficult to satisfy even if $\delta_I=0$,
366 because the heterosynaptic effect on Ca^{2+} dynamics in the spine is expected to be smaller than the
367 homosynaptic effect (i.e. $C_I < C_{pre}$). A similar analysis is possible for E-to-E interaction although the
368 phase diagram becomes complicated in this case (Fig. 4D; see *Methods* for details).

369 These analytical results revealed that the heterosynaptic effects are always observable if
370 the parameters of calcium dynamics fall into a certain region in the parameter space, ensuring the
371 robustness of h-STDP in our framework.

372

373 *h-STDP induces detailed dendritic E/I balance at dendritic hotspots*

374 Results so far suggest that the proposed model gives a good approximation of h-STDP. We next
375 study how this h-STDP rule shapes synaptic organization on the dendrite of a simulated neuron to
376 investigate its possible functions. To this end, we first consider a model of a dendritic hotspot (Jia et
377 al., 2010) that receives 10 excitatory inputs and one inhibitory input (Fig. 5A), because
378 heterosynaptic effect is typically confined within $10\mu m$ from the synapse (Hayama et al., 2013).
379 Excitatory inputs are organized into 5 pairs, and each pair of excitatory synapses receives correlated
380 inputs (Fig. 5B; see *Dendritic hotspot model* in *Methods* for details). In addition, the inhibitory input is
381 correlated with one excitatory pair (in Fig. 5A, blue ones). Here, we assumed that postsynaptic
382 activity follows a Poisson process with a fixed rate, because the influence of a single hotspot to the
383 soma is usually negligible. In addition, we neglected the effect of morphology and hypothesized that
384 heterosynaptic interaction occurs instantaneously within the hotspot. In this configuration,
385 surprisingly, excitatory synapses correlated with the inhibitory input are potentiated while other
386 synapses experience minor depression (Fig. 5C top). As a result, the dendritic membrane potential
387 becomes less correlated with all hidden signals, because strong negative correlation with the blue
388 signal is cancelled by potentiated excitatory inputs, while weak positive correlation with other signals
389 are diminished due to LTD at corresponding excitatory synapses (Fig. 5C bottom). This GABA-driven
390 potentiation is only observable when inhibitory activity is tightly correlated with excitatory activities,
391 and becomes larger when inhibitory spike precedes excitatory spikes compared to the opposite case
392 (Fig. 5D). In addition, we found that when heterosynaptic inhibitory effect γ_I is large enough to causes
393 strong hyperpolarization at nearby synapses, depression is observed at correlated excitatory
394 synapses (blue area in Fig. 5E) instead of potentiation (red area in Fig. 5E). However, as we saw in
395 Figures 3 and 4, such a large inhibitory effect does not reproduce STDP experiments, thus unlikely to

396 be observed in the actual brain. These results indicate that h-STDP induces dendrite-specific
397 detailed E/I balance by potentiating excitatory synapses correlated with inhibitory synapses.

398 To reveal the underlying mechanism of this E/I balance generation, from the simulation
399 data, we calculated the probability of calcium level being above the LTD/LTP thresholds after a
400 presynaptic spike. The probability of LTP occurrence shows similar trajectories after a presynaptic
401 spike, regardless of whether presynaptic activity is correlated with inhibitory input or not (blue and
402 gray dotted lines in Fig. 5F, respectively). On the other hand, the maximum probability of LTD
403 occurrence is significantly lower for spines correlated with inhibitory inputs (blue vs. gray solid line in
404 Fig. 5F), although the probability goes up after the presynaptic spike in both cases. This asymmetry
405 between LTP and LTD can be understood in the following way; LTD is mainly caused when the
406 presynaptic neuron fires at a low firing rate and the postsynaptic neuron remains silent both in the
407 experiment (Malenka and Bear, 2004) and in the model (gray line in Fig. 5G). However, if inhibitory
408 input arrives at a nearby dendrite in coincidence, calcium boost caused by excitatory presynaptic
409 input is attenuated by heterosynaptic inhibitory effect (black line in Fig. 5G). As a result, LTD is
410 shunted by correlated inhibitory inputs. On the other hand, LTP is mainly caused by coincidence
411 between pre and postsynaptic spikes, which induces a large increase in calcium level that
412 overwhelms the attenuation by the heterosynaptic inhibitory effect. Thus, inhibitory activity at a
413 nearby site does not prevent LTP at correlated excitatory synapses (Fig. 5H). Therefore, correlated
414 spines experiences less depression, hence tend to be potentiated as a net sum.

415 To check the generality of the observed dendritic E/I balance, we extended the model to a
416 two-layered single cell (Poirazi et al., 2003) by modeling each branch with one dendritic hotspot (Fig.
417 6A; see *Two-layered neuron model* in *Methods* for details), and investigated the dendritic
418 organization by h-STDP. Here, we introduced 10 ms delay between excitatory and inhibitory

419 stimulation(Froemke, 2015). Even in this case, when the postsynaptic neuron receives input from
420 various neurons with different selectivity, each dendritic hotspot shapes its excitatory synaptic
421 organization based on the selectivity of its inhibitory input (Fig. 6BC; the frame colors of Fig. 6B
422 represent the inhibitory selectivities). As a result, excitatory synapses on the dendritic tree become
423 clustered as observed in previous experiments (Kleindienst et al., 2011)(Takahashi et al., 2012).
424 Note that, in our model, this clustering of excitatory synapses is caused by common inhibitory inputs
425 instead of direct interaction among excitatory spines.

426 We further investigated the possible function of this synaptic organization in information
427 processing. To this end, we consecutively presented the five stimuli to the two-layered neuron model
428 (Fig. 6E). Before the learning, the neuron shows almost constant response to the stimulation with a
429 small dip at the change points (Fig. 6E top). In contrast, after the learning, the neuron shows
430 transient bursting activity immediately after the stimulus is changed to the next one, and rapidly
431 returns to an almost silent state (Fig. 6E middle). Hence, by h-STDP, a neuron can acquire sensitivity
432 toward abrupt changes in stimuli (Fig. 6D and 6E bottom).

433

434 *h-STDP explains critical period plasticity of binocular matching*

435 Results so far indicate that h-STDP induces GABA-driven synaptic reorganization that enriches
436 dendritic computation. To investigate its relationship with the developmental plasticity, we next
437 consider a model of critical period plasticity in binocular matching (Wang et al., 2010)(Wang et al.,
438 2013). In mice, one week after the eye opening, typically, binocular neurons in V1 still have different
439 orientation selectivity for inputs from two eyes. Nevertheless, two more weeks after, selective
440 orientations for both eyes get closer, and eventually they almost coincide with each other (Wang et
441 al., 2010). Moreover, this binocular matching is disrupted by accelerating inhibitory maturation (Wang

442 et al., 2013). Thus, expectedly, activity of inhibitory neurons play a crucial role in binocular matching
443 in addition to Hebbian plasticity at excitatory synapses.

444 We modeled this process with a two-layered single cell model introduced in Figure 6 (Fig.
445 7A right; see *Two-layered neuron model* in *Methods* for details). Input spike trains were modeled as
446 rate modulated Poisson processes driven by a circular variable θ , which corresponds to the direction
447 of moving visual stimuli. We assumed followings: (i) inputs from ipsi- and contralateral eyes already
448 have some weak orientation selectivity at the eye opening (Wang et al., 2010)(Espinosa and Stryker,
449 2012), (ii) Inhibitory cells are driven by both ipsi- and contralateral eyes (Yazaki-Sugiyama et al.,
450 2009)(Kuhlman et al., 2011), (iii) The average selectivity of inhibitory inputs comes in between the
451 selectivity for ipsilateral and contralateral excitatory inputs (Fig. 7A left). The last assumption has not
452 yet been supported from experimental evidence, but if inhibition is provided from neighboring
453 interneurons, these inhibitory neurons are likely to be driven by similar sets of feedforward excitatory
454 inputs to those driving the output neuron. Here, we consider direction selectivity instead of orientation
455 selectivity for mathematical convenience, but the same argument holds for the latter.

456 In the simulation, we first run the process without inhibition then introduced GABAergic
457 inputs after a while (red lines in Fig. 7B,E represent the starting points of inhibitory inputs), because
458 maturation of inhibitory neurons typically occurs in a later stage of the development (Hensch, 2005).
459 Upon the introduction of inhibition, in each branch, the mean preferred direction of excitatory
460 synapses converges to that of the local inhibition owing to heterosynaptic plasticity (Fig. 7B top; see
461 *Methods* for details of evaluation methods), though synaptic weight development was biased toward
462 the selectivity of the postsynaptic neuron (Fig. 7D; here, the bias is toward the right side). This
463 dendritic E/I balancing shrinks the difference between ipsilateral and contralateral selectivity on
464 average, because both of them get closer to the inhibitory selectivity (Fig. 7B middle). As a result,

465 binocular selectivity becomes stronger (Fig. 7B bottom), and the responses for monocular inputs
466 approximately coincide with each other (Fig. 7C right). Deprivation of contralateral inputs
467 immediately after the introduction of inhibition blocks binocular matching (Fig. 7E), as expected from
468 the experiment (Wang et al., 2010).

469 In addition, precocious GABA maturation is known to disrupt binocular matching (Wang et
470 al., 2013). Our model suggests that the disruption is possibly related to the violation of the third
471 assumption in the model. When the direction of the mean inhibitory selectivity is far different from
472 both ipsilateral and contralateral selectivity (in Fig. 7F, at the parameter regions outside of the area
473 surrounded by purple and green lines), h-STDP does not work effectively (Fig. 7F top), and the
474 difference between ipsi- and contralateral inputs is not reduced (Fig. 7F middle). As a result,
475 binocular direction selectivity is not improved by learning (Fig. 7F bottom). These results indicate that
476 GABA-maturation and resultant h-STDP are an important part of the underlying mechanisms of
477 critical period plasticity in binocular matching.

478

479

480 **Discussion**

481 In this study, we first showed that a calcium-based plasticity model robustly captures several
482 characteristics of plasticity-related interaction between neighboring synapses in millisecond
483 timescale, by introducing heterosynaptic interaction terms (Fig. 2-4). Based on this proposed model,
484 we next investigated the possible functions of h-STDP. Our study revealed that h-STDP causes the
485 detailed dendritic E/I balance on dendritic hotspots (Fig. 5,6), which is beneficial for change detection
486 (Fig. 6). Furthermore, we found that h-STDP can induce binocular matching upon GABA maturation,
487 and support an accurate input estimation (Fig. 7).

488 *Experimental predictions*

489 Our study provides three experimental testable predictions: First, our results provide a
490 hypothesis for synaptic organization on dendritic tree. It is known that excitatory synaptic inputs to a
491 dendritic hotspot often show correlated activities (Kleindienst et al., 2011)(Takahashi et al., 2012).
492 Our results indicate that an inhibitory input may also be correlated to excitatory inputs projecting to
493 the nearby dendrite (Fig. 5,6), especially on a dendritic tree of an excitatory neuron that is sensitive
494 to changes in the external environment (Fig. 6,7). Moreover, the model explains why feature
495 selectivity of these spines only shows a weak similarity despite their correlations (Jia et al.,
496 2010)(Chen et al., 2011). When a synaptic cluster is carved by the heterosynaptic effect of common
497 inhibitory inputs, not by excitatory-to-excitatory interactions, variability of feature selectivity within the
498 cluster tends to be large, because inhibitory neurons typically have a wider feature selectivity than
499 excitatory neurons (Ma et al., 2010)(Moore and Wehr, 2013). In addition, it should also be noted that,
500 E-to-E heterosynaptic LTP is typically induced as a meta-plasticity in the timescale of minutes
501 (Harvey and Svoboda, 2007), which itself is not sufficient to create a correlation-based synaptic
502 cluster.

503 Secondly, the results in Figure 5 indicate that LTD at an excitatory synapse is cancelled out
504 by coincident inhibitory inputs to the nearby dendrite. Thus, LTD by low frequency stimuli (Malenka
505 and Bear, 2004) can be attenuated by coincident GABA uncaging around the stimulated spine. Note
506 that this result would not contradict with GABA-driven heterosynaptic LTD observed in paired
507 stimulation, because in that experiment, the excitatory spine was presumably overexcited for
508 inducing LTD in the absence of GABA (Hayama et al., 2013). Indeed, coincident GABAergic inputs
509 may induce heterosynaptic LTD if combined with presynaptic stimulation at a moderately high
510 frequency that itself does not cause LTD (Blaise and Bronzino, 2003).

511 The third implication of the model is about binocular matching. Our model indicates that
512 GABA-maturation plays a critical role in binocular matching, and proposes a candidate mechanism
513 for disruption of binocular matching by precocious GABA maturation (Wang et al., 2013)(Fig. 7).
514 However, the phenomenon can also be explained by Hebbian plasticity plus some kind of
515 meta-plasticity. If binocular matching is purely induced by Hebbian plasticity not through
516 heterosynaptic mechanism, selective orientation after the matching should depend solely on the
517 initial selectivity for monocular inputs, assuming that selectivity of presynaptic neurons remains the
518 same. Especially when the contralateral input is larger than the ipsilateral input, the resultant
519 selectivity should approximately coincide with the original contralateral selectivity. On the other hand,
520 if the proposed mechanism takes part in the development, the consequent selectivity should also be
521 influenced by the mean selectivity of inhibitory input neurons. Thus, long-term imaging of monocular
522 selectivity at binocular neurons in V1 would reveal whether a covariance-based rule is sufficient
523 enough to explain the phenomena, or some other mechanisms including the proposed one also play
524 a major role in the shift.

525

526 *Carrier of heterosynaptic interaction*

527 Heterosynaptic plasticity has been observed in various spatial and temporal scales, and arguably
528 underlying molecular mechanisms are different for different spatiotemporal scales (Nishiyama and
529 Yasuda, 2015). In the case of milliseconds-order interaction, single-atomic ions are strong
530 candidates, because poly-atomic ions such as IP_3 are too big to move rapidly from spine to spine
531 (Santamaria et al., 2006). Suppose that changes in Ca^{2+} concentration at an un-stimulated spine are
532 crucial for heterosynaptic plasticity, Ca^{2+} influx/outflux from either intra or extracellular sources are
533 necessary for induction of heterosynaptic plasticity. Because inhibitory synaptic inputs often change

534 the local Ca^{2+} concentration in the dendritic branch (Müllner et al., 2015), intracellular spreading of
535 Ca^{2+} may be a major source for Ca^{2+} changes in nearby un-stimulated spines. At the same time,
536 because inhibitory inputs significantly modulate the membrane voltage of local dendrite (Gidon and
537 Segev, 2012), a synaptic input should strongly drive Ca^{2+} influx/outflux through NMDA and VDCC
538 from extracellular sources even at nearby un-stimulated spines. In addition, most of intracellular
539 calcium-ions exist within calcium-buffer (Higley and Sabatini, 2012), and arguably they are also
540 important for induction of synaptic plasticity. In our model, both current-based interaction (*Spine*
541 *model*) and calcium-based interaction (*Reduced model*) replicate the experimental results (Fig. 2 and
542 4, respectively). Nevertheless, our analytical study suggest that the heterosynaptic Ca^{2+} change
543 typically needs to be comparable with the homosynaptic change in order to cause significant
544 heterosynaptic plasticity through calcium-based interaction (Fig. 4C, D). Thus, our study implies
545 possible importance of current-based interaction and spine specific influx/outflux of extracellular Ca^{2+}
546 for heterosynaptic plasticity.

547 Note that heterosynaptic interaction does not need to work in milliseconds order to interfere
548 with STDP. For instance, E-to-E heterosynaptic LTD can be initiated by spreading of LTD-related
549 molecules, not by messengers of neural activity (Hayama et al., 2013). In addition, for a shift in STDP
550 time window, changes in the ratio between calcium influx through NMDA and the influx through
551 VDCC possibly play a crucial role (Paille et al., 2013).

552

553 *Inhibitory cell types*

554 Somatostatin positive (SOM^+) inhibitory neurons are typically projected to the apical dendrite, their
555 IPSP curves is shorter than the timescales of NMDA or Ca^{2+} dynamics (Markram et al., 2004), and
556 they often show strong feature selectivity compared to other inhibitory neuron types (Ma et al., 2010).

557 Thus, this inhibitory cell type is the likely candidate for heterosynaptic STDP. However, our results do
558 not exclude parvalbumin positive (PV⁺) inhibitory neurons, which usually have projections to proximal
559 dendrites, and also are typically fast spiking (Markram et al., 2004). In particular, h-STDP through
560 PV⁺ cell may play important roles in critical period plasticity (Takesian and Hensch, 2013).

561

562 *Related theoretical studies*

563 Previous biophysical simulation studies revealed that synaptic plasticity at excitatory synapse
564 critically depends on inhibitory inputs at nearby dendrite (Cutsuridis, 2011)(Bar-Ilan et al.,
565 2013)(Jedlicka et al., 2015), but these studies did not reveal much of the functional roles of the
566 heterosynaptic plasticity. On the other hands, network modeling studies found that heterosynaptic
567 plasticity provides a homeostatic mechanism (Chen et al., 2013)(Zenke et al., 2015), but in these
568 models, heterosynaptic plasticity was modeled as a global homeostatic plasticity without any branch
569 specificity, and the advantage over other homeostatic mechanisms was unclear. In this study, by
570 considering intermediate abstraction with analytical but biologically plausible models, we proposed
571 candidate mechanisms for experimental results that have not been modeled before, and revealed
572 potential functions of h-STDP in neural circuit formation.

573

574

575 **References**

- 576 Bar-Ilan L, Gidon A, Segev I (2013) The role of dendritic inhibition in shaping the plasticity of
577 excitatory synapses. *Front Neural Circuits* 6.
- 578 Bazelot M, Bocchio M, Kasugai Y, Fischer D, Dodson PD, Ferraguti F, Capogna M (2015)
579 Hippocampal Theta Input to the Amygdala Shapes Feedforward Inhibition to Gate

- 580 Heterosynaptic Plasticity. *Neuron* 87:1290–1303.
- 581 Bi GQ, Poo MM (1998) Synaptic modifications in cultured hippocampal neurons: dependence on
582 spike timing, synaptic strength, and postsynaptic cell type. *J Neurosci Off J Soc Neurosci*
583 18:10464–10472.
- 584 Blaise JH, Bronzino JD (2003) Effects of stimulus frequency and age on bidirectional synaptic
585 plasticity in the dentate gyrus of freely moving rats. *Exp Neurol* 182:497–506.
- 586 Branco T, Clark BA, Häusser M (2010) Dendritic Discrimination of Temporal Input Sequences in
587 Cortical Neurons. *Science* 329:1671–1675.
- 588 Caporale N, Dan Y (2008) Spike Timing–Dependent Plasticity: A Hebbian Learning Rule. *Annu Rev*
589 *Neurosci* 31:25–46.
- 590 Chen J-Y, Lonjers P, Lee C, Chistiakova M, Volgushev M, Bazhenov M (2013) Heterosynaptic
591 Plasticity Prevents Runaway Synaptic Dynamics. *J Neurosci* 33:15915–15929.
- 592 Chen X, Leischner U, Rochefort NL, Nelken I, Konnerth A (2011) Functional mapping of single
593 spines in cortical neurons in vivo. *Nature* 475:501–505.
- 594 Cutsuridis V (2011) GABA inhibition modulates NMDA-R mediated spike timing dependent plasticity
595 (STDP) in a biophysical model. *Neural Netw* 24:29–42.
- 596 Dorn AL, Yuan K, Barker AJ, Schreiner CE, Froemke RC (2010) Developmental sensory experience
597 balances cortical excitation and inhibition. *Nature* 465:932–936.
- 598 Espinosa JS, Stryker MP (2012) Development and Plasticity of the Primary Visual Cortex. *Neuron*
599 75:230–249.
- 600 Froemke RC (2015) Plasticity of Cortical Excitatory-Inhibitory Balance. *Annu Rev Neurosci* 38:195–
601 219.
- 602 Gambino F, Pagès S, Kehayas V, Baptista D, Tatti R, Carleton A, Holtmaat A (2014)

- 603 Sensory-evoked LTP driven by dendritic plateau potentials in vivo. *Nature* 515:116–119.
- 604 Gerstner W, Kempter R, van Hemmen JL, Wagner H (1996) A neuronal learning rule for
605 sub-millisecond temporal coding. *Nature* 383:76–81.
- 606 Gidon A, Segev I (2012) Principles Governing the Operation of Synaptic Inhibition in Dendrites.
607 *Neuron* 75:330–341.
- 608 Graupner M, Brunel N (2007) STDP in a Bistable Synapse Model Based on CaMKII and Associated
609 Signaling Pathways. *PLoS Comput Biol* 3:e221.
- 610 Graupner M, Brunel N (2012) Calcium-based plasticity model explains sensitivity of synaptic
611 changes to spike pattern, rate, and dendritic location. *Proc Natl Acad Sci* 109:3991–3996.
- 612 Harvey CD, Svoboda K (2007) Locally dynamic synaptic learning rules in pyramidal neuron dendrites.
613 *Nature* 450:1195–1200.
- 614 Hayama T, Noguchi J, Watanabe S, Takahashi N, Hayashi-Takagi A, Ellis-Davies GCR, Matsuzaki
615 M, Kasai H (2013) GABA promotes the competitive selection of dendritic spines by controlling
616 local Ca²⁺ signaling. *Nat Neurosci* 16:1409–1416.
- 617 Hensch TK (2005) Critical period plasticity in local cortical circuits. *Nat Rev Neurosci* 6:877–888.
- 618 Higley MJ, Sabatini BL (2012) Calcium Signaling in Dendritic Spines. *Cold Spring Harb Perspect Biol*
619 4:a005686.
- 620 Hiratani N, Fukai T (2015) Mixed Signal Learning by Spike Correlation Propagation in Feedback
621 Inhibitory Circuits. *PLoS Comput Biol* 11:e1004227.
- 622 Jedlicka P, Benuskova L, Abraham WC (2015) A Voltage-Based STDP Rule Combined with Fast
623 BCM-Like Metaplasticity Accounts for LTP and Concurrent “Heterosynaptic” LTD in the Dentate
624 Gyrus In Vivo. *PLOS Comput Biol* 11:e1004588.
- 625 Jia H, Rochefort NL, Chen X, Konnerth A (2010) Dendritic organization of sensory input to cortical

- 626 neurons in vivo. *Nature* 464:1307–1312.
- 627 Kleindienst T, Winnubst J, Roth-Alpermann C, Bonhoeffer T, Lohmann C (2011) Activity-Dependent
628 Clustering of Functional Synaptic Inputs on Developing Hippocampal Dendrites. *Neuron*
629 72:1012–1024.
- 630 Koch C (1998) *Biophysics of Computation: Information Processing in Single Neurons*. Oxford
631 University Press.
- 632 Kuhlman SJ, Tring E, Trachtenberg JT (2011) Fast-spiking interneurons have an initial orientation
633 bias that is lost with vision. *Nat Neurosci* 14:1121–1123.
- 634 Liu G (2004) Local structural balance and functional interaction of excitatory and inhibitory synapses
635 in hippocampal dendrites. *Nat Neurosci* 7:373–379.
- 636 London M, Häusser M (2005) Dendritic Computation. *Annu Rev Neurosci* 28:503–532.
- 637 Lüscher C, Malenka RC (2012) NMDA Receptor-Dependent Long-Term Potentiation and Long-Term
638 Depression (LTP/LTD). *Cold Spring Harb Perspect Biol* 4:a005710.
- 639 Malenka RC, Bear MF (2004) LTP and LTD: An Embarrassment of Riches. *Neuron* 44:5–21.
- 640 Mallet N, Moine CL, Charpier S, Gonon F (2005) Feedforward Inhibition of Projection Neurons by
641 Fast-Spiking GABA Interneurons in the Rat Striatum In Vivo. *J Neurosci* 25:3857–3869.
- 642 Markram H, Toledo-Rodriguez M, Wang Y, Gupta A, Silberberg G, Wu C (2004) Interneurons of the
643 neocortical inhibitory system. *Nat Rev Neurosci* 5:793–807.
- 644 Ma W, Liu B, Li Y, Huang ZJ, Zhang LI, Tao HW (2010) Visual Representations by Cortical
645 Somatostatin Inhibitory Neurons—Selective But with Weak and Delayed Responses. *J Neurosci*
646 30:14371–14379.
- 647 Mel BW, Schiller J (2004) On the Fight Between Excitation and Inhibition: Location Is Everything. *Sci*
648 *Signal* 2004:pe44–pe44.

- 649 Moore AK, Wehr M (2013) Parvalbumin-Expressing Inhibitory Interneurons in Auditory Cortex Are
650 Well-Tuned for Frequency. *J Neurosci* 33:13713–13723.
- 651 Müllner FE, Wierenga CJ, Bonhoeffer T (2015) Precision of Inhibition: Dendritic Inhibition by
652 Individual GABAergic Synapses on Hippocampal Pyramidal Cells Is Confined in Space and
653 Time. *Neuron* 87:576–589.
- 654 Nishiyama J, Yasuda R (2015) Biochemical Computation for Spine Structural Plasticity. *Neuron*
655 87:63–75.
- 656 Oh WC, Parajuli LK, Zito K (2015) Heterosynaptic Structural Plasticity on Local Dendritic Segments
657 of Hippocampal CA1 Neurons. *Cell Rep* 10:162–169.
- 658 Paille V, Fino E, Du K, Morera-Herreras T, Perez S, Kotaleski JH, Venance L (2013) GABAergic
659 Circuits Control Spike-Timing-Dependent Plasticity. *J Neurosci* 33:9353–9363.
- 660 Petersen CCH, Malenka RC, Nicoll RA, Hopfield JJ (1998) All-or-none potentiation at CA3-CA1
661 synapses. *Proc Natl Acad Sci* 95:4732–4737.
- 662 Poirazi P, Brannon T, Mel BW (2003) Pyramidal Neuron as Two-Layer Neural Network. *Neuron*
663 37:989–999.
- 664 Santamaria F, Wils S, De Schutter E, Augustine GJ (2006) Anomalous Diffusion in Purkinje Cell
665 Dendrites Caused by Spines. *Neuron* 52:635–648.
- 666 Shouval HZ, Bear MF, Cooper LN (2002) A unified model of NMDA receptor-dependent bidirectional
667 synaptic plasticity. *Proc Natl Acad Sci* 99:10831–10836.
- 668 Song S, Miller KD, Abbott LF (2000) Competitive Hebbian learning through spike-timing-dependent
669 synaptic plasticity. *Nat Neurosci* 3:919–926.
- 670 Takahashi N, Kitamura K, Matsuo N, Mayford M, Kano M, Matsuki N, Ikegaya Y (2012) Locally
671 Synchronized Synaptic Inputs. *Science* 335:353–356.

- 672 Takesian AE, Hensch TK (2013) Balancing plasticity/stability across brain development. *Prog Brain*
673 *Res* 207:3–34.
- 674 Tsukada M, Aihara T, Kobayashi Y, Shimazaki H (2005) Spatial analysis of spike-timing-dependent
675 LTP and LTD in the CA1 area of hippocampal slices using optical imaging. *Hippocampus*
676 15:104–109.
- 677 Vogels TP, Sprekeler H, Zenke F, Clopath C, Gerstner W (2011) Inhibitory Plasticity Balances
678 Excitation and Inhibition in Sensory Pathways and Memory Networks. *Science* 334:1569–1573.
- 679 Wang B-S, Feng L, Liu M, Liu X, Cang J (2013) Environmental Enrichment Rescues Binocular
680 Matching of Orientation Preference in Mice that Have a Precocious Critical Period. *Neuron*
681 80:198–209.
- 682 Wang B-S, Sarnaik R, Cang J (2010) Critical Period Plasticity Matches Binocular Orientation
683 Preference in the Visual Cortex. *Neuron* 65:246–256.
- 684 Wilson NR, Ty MT, Ingber DE, Sur M, Liu G (2007) Synaptic Reorganization in Scaled Networks of
685 Controlled Size. *J Neurosci* 27:13581–13589.
- 686 Yazaki-Sugiyama Y, Kang S, Câteau H, Fukai T, Hensch TK (2009) Bidirectional plasticity in
687 fast-spiking GABA circuits by visual experience. *Nature* 462:218–221.
- 688 Zenke F, Agnes EJ, Gerstner W (2015) Diverse synaptic plasticity mechanisms orchestrated to form
689 and retrieve memories in spiking neural networks. *Nat Commun* 6.

690

691 **Legends**

692 **Figure 1:** Schematic figure of the model of heterosynaptic spike-timing-dependent plasticity
693 (h-STDP).

694 **A)** A schematic figure of the model. Two variables in the spine $u(t)$ and $c(t)$ represent the normalized

695 membrane potential and Ca^{2+} concentration respectively. Presynaptic action potentials modulate the
696 membrane potential $u(t)$ through AMPA (x^A) and NMDA ($g_N(u)x^N$) receptors. In addition, $u(t)$ is
697 modified by back-propagation (x^{BP}), and heterosynaptic current caused by excitatory (x^E) and
698 inhibitory (x^I) inputs. Calcium level $c(t)$ is modulated by influx/outflux through NMDA ($g_N(u)x^N$) and
699 VDCC ($g_V(u)$). Consequently, $c(t)$ is indirectly controlled by $u(t)$ because both NMDA and VDCC are
700 voltage-dependent. **B)** An example of dynamics of the membrane potential variable $u(t)$ (top), Ca^{2+}
701 concentration $c(t)$ (middle), and the intermediate variable $y(t)$ that controls the synaptic weight
702 $w(t)$ (bottom). Change in the Ca^{2+} level roughly follows the membrane potential dynamics, and the
703 intermediate variable $y(t)$ is positively (negatively) modulated when Ca^{2+} level is above LTP(LTD)
704 thresholds represented by orange(cyan) dotted lines. Based on the intermediate variable $y(t)$,
705 synaptic weight $w(t)$ is updated in a slow timescale (see Figure 5C for example).

706

707 **Figure 2:** The model reproduces spike-timing-dependent heterosynaptic effects.

708 **A)** Spike timing window with/without a di-synaptic GABAergic input. Lines are simulation data, and
709 points are experimental data taken from (Paille et al., 2013). Vertical dotted lines represent the
710 spike-timing differences at which Panel **B** was calculated. **B)** Dynamics of calcium concentration $c(t)$
711 (top) and the intermediate variable $y(t)$ (bottom) at the stimulated spine. Gray areas in the bottom
712 figures represent the regions satisfying $y(t) < y_{th}/K_{rep}$, in which the change in the intermediate is not
713 reflected into synaptic weight, where K_{rep} represents the number of paired stimulation given in the
714 simulation for Panel **A**. **C)** Synaptic weight change with/without GABAergic inputs right before
715 pre/post stimulation. Data points were taken from (Hayama et al., 2013). The cyan point is a result
716 from muscimol application, not GABA uncaging. **D)** Dynamics of $c(t)$ and $y(t)$ at the stimulated spine
717 (blue lines) and a neighboring spine (green lines). Solid lines represent the dynamics under GABA

718 uncaging, and dotted lines are the controls. Note that in the left panel, fractions of blue lines are
719 hidden under green lines, because postsynaptic and inhibitory heterosynaptic inputs cause the same
720 dynamics in both stimulated and neighboring spines.

721

722 **Figure 3:** Parametric robustness of h-STDP model.

723 **A)** Mean squared fitting errors for the model of the striatum experiment at various values of model
724 parameters. In each panel, all other parameters were fixed, and the white mark represents the value
725 used in Figure 2. See *Methods* for the definitions of parameters. **B)** Comparison of parametric
726 dependence of models fitted for the results from the striatum and CA1 experiments. Vertical dotted
727 lines represent the value used in Figure 2. NMDA/AMPA ratio in the bottom panel was calculated as
728 $\gamma_N \tau_N / \gamma_A \tau_A$ at various values of γ_N . Note that the fluctuation in blue lines was caused by
729 double-threshold dynamics of the model, not by noise.

730

731 **Figure 4:** Phase transitions on STDP time window in an analytical model of h-STDP.

732 **A, B)** STDP windows at various strength of heterosynaptic inhibitory effect C_I . Panel **A** corresponds
733 to the striatum experiment, and Panel **B** corresponds to the CA1 experiment. Top and bottom figures
734 in Panel **B** represent the stimulated and a neighbor spine, respectively. Note that values in Panel **B**
735 were calculated by $\tilde{y} = \text{sgn}(y) \cdot [|y| - 15]_+$ to reflect the effect of thresholding. **C)** Phase diagram of
736 STDP time window calculated for inhibitory effect C_I and LTP threshold θ_p . Colors show the number
737 of local minimum/maximum, and lines are typical STDP time windows at each phase. Parameters
738 written on the right side (top) of the panel represent the critical values of θ_p (C_I). **D)** Phase diagram
739 calculated for heterosynaptic excitatory effect parameter C_E and postsynaptic effect parameters C_{post}
740 at a fixed inhibitory effect ($C_I=0.5$). See *Reduced model* in *Methods* for details.

741 **Figure 5:** Emergence of detailed dendritic excitatory/inhibitory balance by h-STDP.

742 **A)** A schematic figure of a dendritic hotspot model. The shaft synapse represents an inhibitory input.

743 Colors represent spike correlation between synaptic inputs. **B)** Examples of correlated spike inputs.

744 Each Raster plot was calculated from 50 simulation trials. **C)** Changes in synaptic weight w (top) and

745 the correlation between the dendritic membrane potential and hidden signals (bottom) under h-STDP.

746 The blue lines represent dynamics of synapses correlated with the inhibitory input. **D)** Synaptic

747 weight change at the excitatory synapses correlated with the inhibitory inputs (blue) and at other

748 synapses (gray), at various inhibitory delays. Error bars in Panels **C** and **D** represent standard

749 deviations over 50 simulation trials. **E)** Relative weight changes w_R calculated at various parameters.

750 We defined w_R by $\langle w_i^E \rangle_{i \in \text{corr}} - \langle w_i^E \rangle_{i \in \text{un-corr}}$, where "corr" represents a set of excitatory synapses

751 correlated with the inhibitory synapse, and "un-corr" stands for uncorrelated ones. Here, weights

752 were calculated by taking average over 10 simulations. **F)** Probability of LTP/LTD occurrence after a

753 presynaptic spike calculated from a simulation. Lines represent the mean LTP/LTD probabilities at

754 excitatory synapses correlated with the inhibitory input (blue lines) and other synapses (gray lines),

755 respectively. **G, H)** Results in single-spike simulations. E/I coincidence prevents LTD effect due to

756 pre-spike (**G**), without affecting LTP effect due to pre-post coincidence (**H**). In Panel **G**, inhibitory

757 spikes were provided at $t=0$ in the black line, $t=-100\text{ms}$ in the gray line, and the excitatory presynaptic

758 spike was given at $t=0$ in both lines. Similarly, in Panel **H**, postsynaptic spikes were provided at $t=-75$

759 (light-gray), 0 (black), $+75\text{ms}$ (dark-gray), and the presynaptic spike was given at $t=0$ in all lines.

760

761 **Figure 6:** Detailed dendritic excitatory/inhibitory balance in a two-layered single cell model.

762 **A)** A schematic illustration of the single cell model. The actual model has 100 dendritic branches

763 each receiving 10 excitatory inputs and 1 inhibitory input. As in Figure 5A, inhibitory inputs are

764 represented by shaft synapses. **B)** Examples of synaptic weight change at each branch. The color of
765 the frames represents the selectivity of the inhibitory input to the branch. Each row represents a
766 different simulation trial. **C)** Mean synaptic weight dynamics of synapses correlated to the local
767 inhibitory inputs, and other synapses. **D)** The ratio of change detecting spikes before and after
768 learning. The ratio was defined as the fraction of spikes occurs within 50 milliseconds from a change
769 in stimuli to the total. In the x-axis, in addition to the mean excitatory input firing rates, the mean
770 inhibitory input firing rates were also modulated from 50 Hz to 210Hz correspondingly to keep the E/I
771 balance of the input. **E)** Raster plots of output spikes before (top) and after (middle) learning, and
772 their firing rate dynamics (bottom), averaged over 100 trials each for 10 simulated neurons. Colors of
773 spikes in the Raster plots represent results from different simulation trials. Black vertical lines
774 represent the change points of excitatory inputs, and horizontal colored bars at the top of the bottom
775 panel corresponds to the colors of presynaptic neurons active in each period. We introduced 10
776 milliseconds delay between excitatory and inhibitory stimulus both during learning (panel **B** and **C**)
777 and in the change detecting task (panel **D** and **E**). The averages in panel **C** and **D** were taken over 10
778 simulation trials.

779

780 **Figure 7:** h-STDP can trigger binocular matching.

781 **A)** (left): Direction selectivity of input neurons. In the model, as depicted by black vertical lines,
782 majorities of excitatory input neurons from the contralateral (ipsilateral) eye are selective for
783 directions around $\theta = -\pi/4$ ($\theta = \pi/4$), while inputs from the inhibitory neurons are weakly selective
784 for $\theta = 0$. (right): A schematic figure of model configuration. Each dendritic branch receives inputs
785 from both ipsi- and contralateral driven excitatory neurons and also from inhibitory neurons. **B)** (top):
786 Difference between mean excitatory direction selectivity and inhibitory direction selectivity in each

787 branch. (middle): Difference between mean ipsi-driven excitatory direction selectivity and mean
788 contra-driven excitatory direction selectivity over all synapses on the neuron. (bottom): Direction
789 selectivity index (DSI) calculated for contralateral inputs (purple), ipsilateral inputs (light-green;
790 hidden under the purple line), and binocular inputs (black). See *Neuron model* in *Methods* for the
791 details of evaluation methods. Red vertical lines represent the timing for introduction of inhibitory
792 inputs. Throughout Figure 7, error bars are standard deviations over 10 simulation trials. **C**) Firing
793 responses of the neuron for monocular inputs, right after the initiation of inhibitory inputs (left;
794 $t=30\text{min}$), and after the learning (right; $t=60\text{min}$). **D**) Examples of direction selectivity of three
795 representative branches before (gray lines; $t=0\text{min}$) and after (purple/light-green lines; $t=60\text{min}$) the
796 learning. Black lines represent the selectivity of the inhibitory input to the branch. **E**) Behavior in
797 monocular deprivation model. In shadowed areas, to mimic monocular deprivation, contra-driven
798 inputs were replaced with rate-fixed Poisson inputs. Ordinates are the same with Panel **B**. **F**)
799 Synaptic weights development at different mean inhibitory selectivity. Ordinates are the same with
800 Panel **B**, and values were calculated at $t=60\text{min}$. Purple and green vertical dotted lines are mean
801 selectivity of contra- and ipsilateral excitatory inputs, respectively.

802

803

804

805 **Table 1. Definitions of variables**

$u_i(t)$	Membrane potential at spine i	Eq. 1
$c_i(t)$	Calcium concentration at spine i	Eq. 3
$y_i(t)$	Intermediate factor (interim synaptic weight)	Eq. 4
$w_i(t)$	Synaptic weight of spine i	Eq. 5
$g_N(u)$	Voltage dependence of NMDA receptor	$g_N(u_i) = \alpha_N u_i + \beta_N$
$g_V(u)$	Voltage dependence of VDCC	$g_V(u_i) = \alpha_V u_i$
$x_i^A(t)$	Inputs through AMPA receptor	Eq. 2 (Q=A)
$x_i^N(t)$	Inputs through NMDA receptor	Eq. 2 (Q=N)
$x_i^{BP}(t)$	Back propagation	Eq. 2 (Q=BP)
$x_i^E(t)$	Excitatory heterosynaptic inputs	Eq. 2 (Q=E)
$x_i^I(t)$	Inhibitory heterosynaptic inputs	Eq. 2 (Q=I)
$u_b^k(t)$	Membrane potential at dendritic branch k	$u_b^k(t) = \sum_{i=1}^{N_b^E} w_i^k u_i^k(t) / (w_o^E N_b^E)$
$u_{soma}(t)$	Membrane potential at the soma	$u_{soma}(t) = \sum_k g_b(u_b^k(t))$
$g_b(u)$	Dendritic nonlinearity function	$g_b(u) = \begin{cases} u & (\text{if } u > u_b^o) \\ u_b^o & (\text{otherwise}) \end{cases}$

806

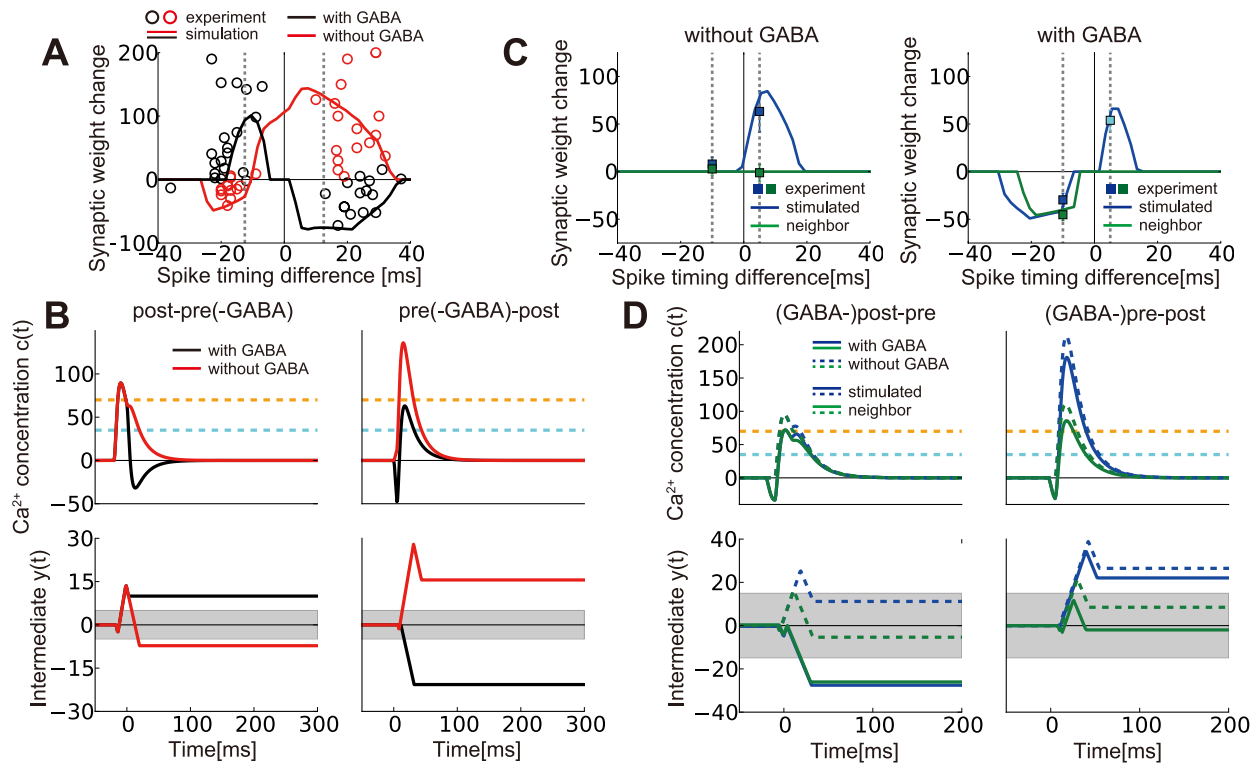


Figure 2:

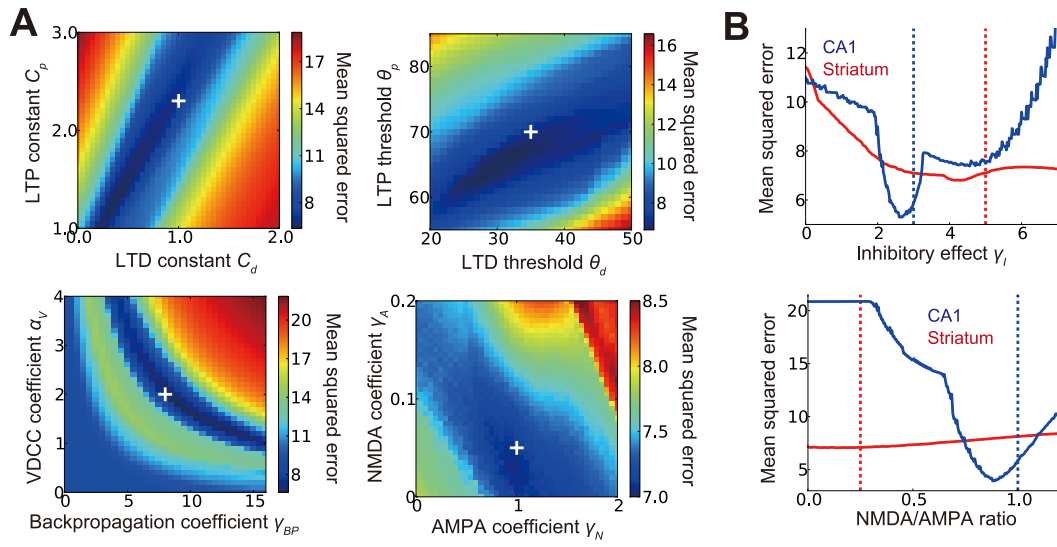


Figure 3:

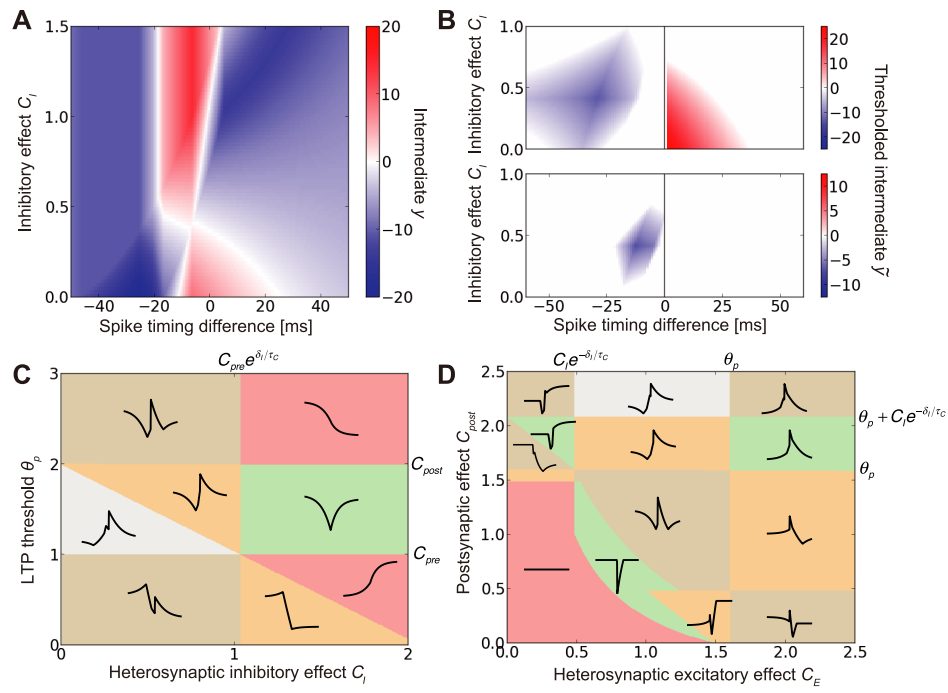


Figure 4:

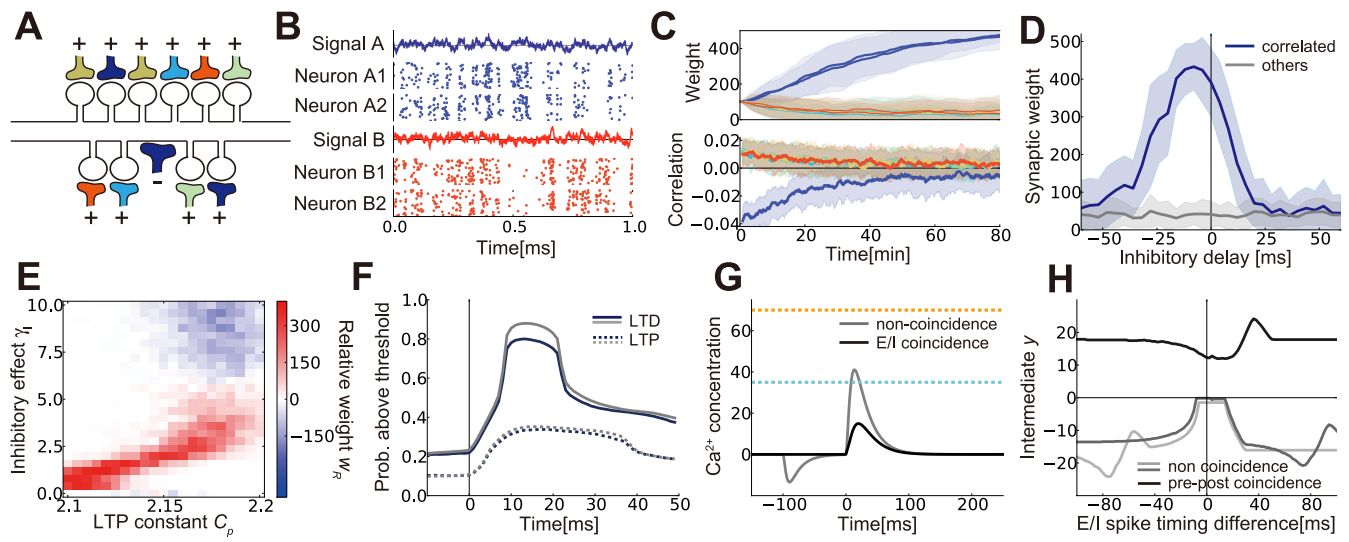


Figure 5:

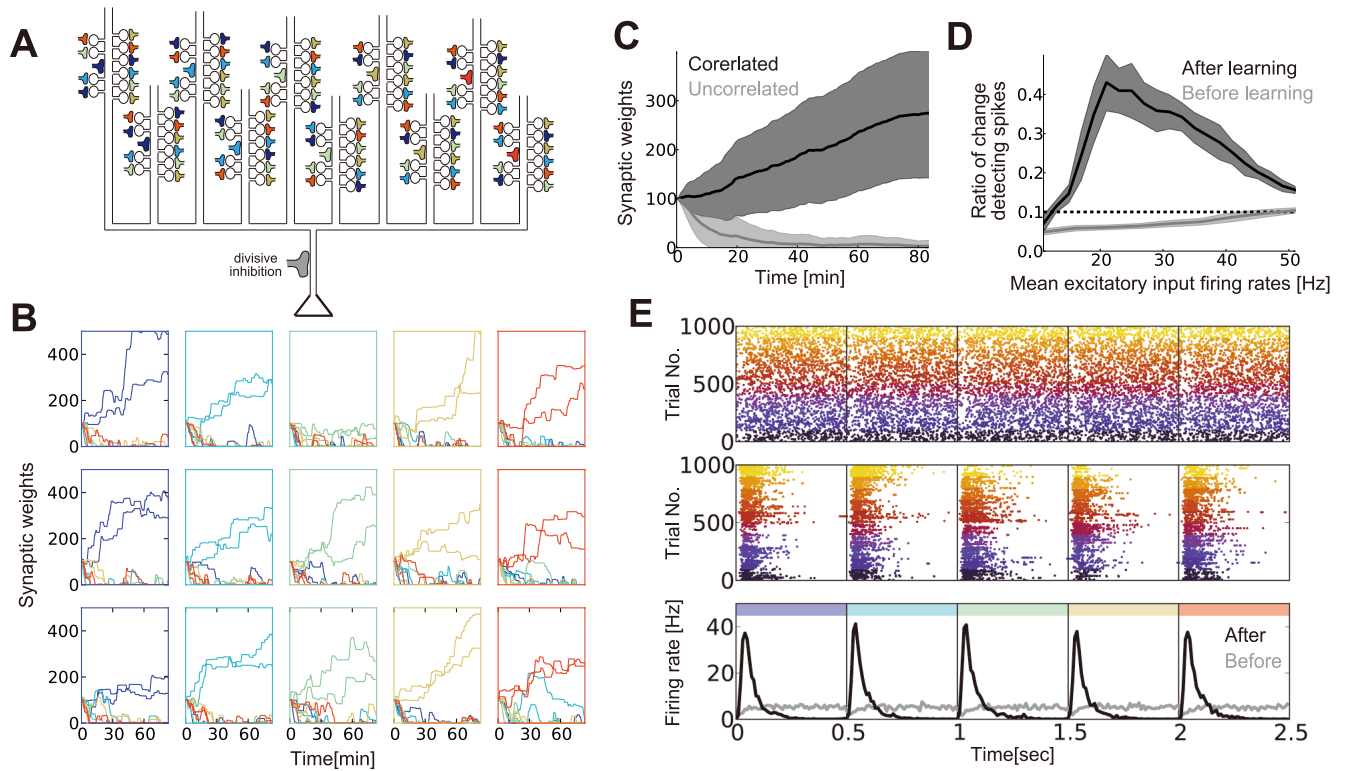


Figure 6:

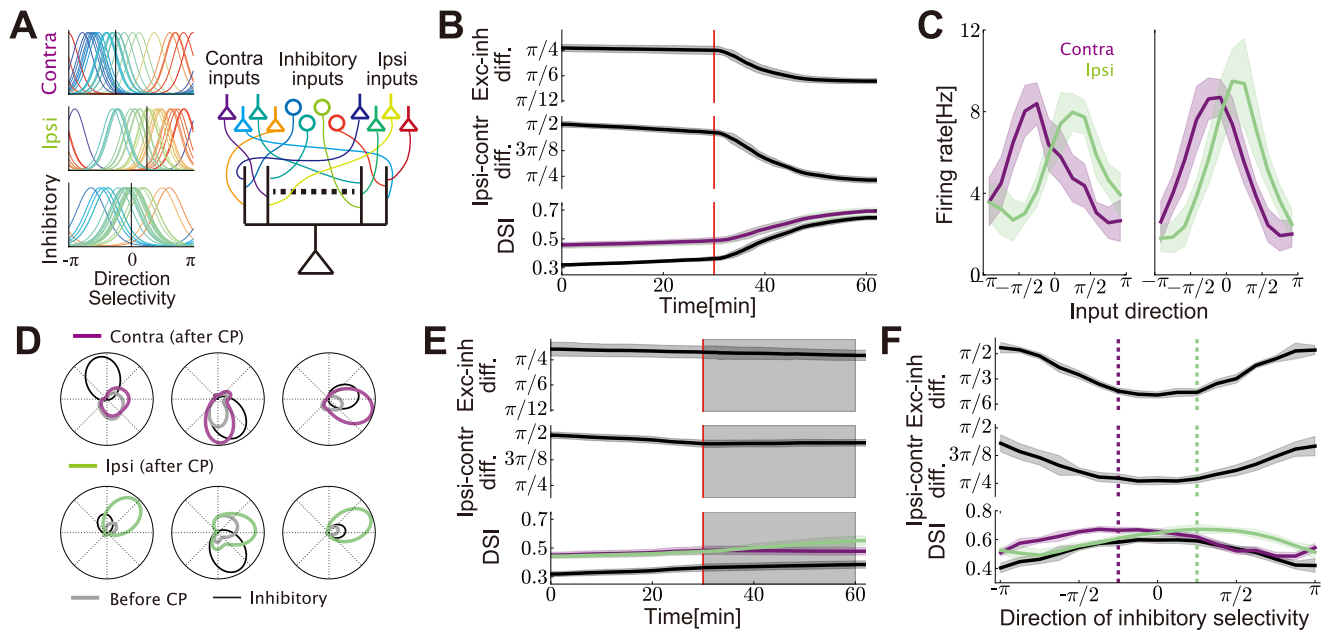


Figure 7: